Machine-learned Decision Trees for Predicting Gold Nanorod Sizes from Spectra

Katsuya Shiratori[1*], Logan D.C. Bishop[2*], Behnaz Ostovar[3], Rashad Baiyasi[3], Yi-Yu Cai[2,†], Peter J. Rossky[2,4,5], Christy F. Landes[2,3,4,5], and Stephan Link[2,3,5]

[1]Applied Physics Graduate Program, [2]Department of Chemistry, [3]Department of Electrical and Computer Engineering, [4]Department of Chemical and Biomolecular Engineering, [5]Smalley Curl Institute, Rice University, 6100 Main Street, Houston, Texas 77005, USA.

Abstract

Electron microscopy is often required in order to precisely correlate the size and shape of plasmonic nanoparticles with their optical properties. Eliminating the need for electron microscopy is one crucial step towards *in situ* sensing applications, especially for complicated sample conditions such as during irreversible chemical reactions or when particles are embedded in a matrix. Here, we show that a machine learning decision tree can accurately predict gold nanorod dimensions over a wide range of sizes. The model is trained using ~450 nanorod geometries and corresponding scattering spectra obtained from finite-difference time-domain simulations. We test the model using a set of experimental spectra and sizes obtained from correlated scanning electron microscopy images, resulting in predictions of the dimensions of gold nanorods within ~10% of their true value (root mean squared percentage error) over a large range of sizes. Analysis of the decision tree structure reveals that a simple correlation with resonance energy and linewidth of the localized surface plasmon resonance is sufficient to predict nanorod dimensions, notably outperforming more complicated models. Our findings illustrate the advantages of using simple machine learning models to infer single particle structural features from their optical spectra.

Introduction

Plasmonic metal nanoparticles are effective candidates for photovoltaic energy conversion,[1-4] photocatalytic reactions,[5-8] and surface-enhanced spectroscopies.[9-12] The collective oscillation of the conduction band electrons, also known as the localized surface plasmon resonance, boosts the signal of scattering and absorption by enhancing the electromagnetic fields around and inside the nanoparticle.[13, 14] Anisotropic nanoparticles like gold nanorods (AuNRs) have two plasmon resonance peaks corresponding to longitudinal and transverse modes. The longitudinal mode can be tuned by varying the aspect ratio and overall size of AuNRs, as the localized surface plasmon resonance is strongly linked to rod morphology[15-22]. The strong relationship between AuNR size and optical properties makes sensing applications attractive, but most synthesis methods generate distributions of morphologies, necessitating characterization before translation of such products to applications.[23-25] By developing *in situ* optical approaches for real time size determination, independent verification of AuNR morphological features could be eliminated.

Characterizing AuNRs requires electron microscopy and spectroscopic measurements. If carried out on the ensemble level, mean AuNR dimensions are related to averaged plasmon resonance maxima.[24] Precise connections between AuNR morphology and optical properties are achieved using single particle spectroscopy correlated with electron microscopy of the same individual AuNRs.[26-28] This approach is time-consuming and often destructive to the sample,[29, 30] and cannot be used when a process induces irreversible morphological changes. Sönnichsen and coworkers showed that it is possible to overcome these challenges using a numerical method to estimate the size of AuNRs from their measured optical spectra based on a database consisting of simulated spectra and their corresponding sizes.[31] Their method predicts AuNR sizes with widths

up to 50 nm. For large AuNRs, radiation damping significantly broadens the spectral linewidths and phase retardation redshifts the resonance maxima.[18, 32-35] This work, however, demonstrates the strong potential for the use of estimation methods that compensate for correlations between spectral features and morphological structure.[31]

Implementation of machine learning (ML) in nanoscience experiments, sometimes called nanoinformatics, takes advantages of experimental/simulated data patterns for prediction and classification.[36, 37] In recent years, ML has been used to characterize heterogeneous catalysts[38-41] and metallic nanostructures,[42-50] as well as to optimize their structural parameters for desired optical properties.[51-54] He *et al.*[55] demonstrated that deep neural networks can predict the size of nanoparticles after training and testing with more than 2000 simulated spectra. Pashkov *et al.*[49] utilized supervised ML for the parametrization of the simulated UV-vis spectra of gold nanospheres and nanorods as a function of particle morphology. One avenue for simplifying characterization of AuNR dimensions is to use ML models trained on simulated spectra to predict experimental data. A simple model, such as a decision tree, is suitable due to ease of implementation, interpretation, and visualization.[56-58] Training a decision tree can draw connections between experimental features and structural properties that are difficult or impossible to collect from a relatively small amount of simulated training data, potentially eliminating the need for time-consuming correlated electron microscopy.

In this paper, we train a decision tree regressor (DTR) using a dataset of ~450 finite-difference time-domain (FDTD) simulated spectra to correlate the linewidth (Γ) and the resonance energy (E_{res}) with AuNR width and length. When validated on simulated FDTD spectra, 90% of all predicted AuNR dimensions are within a relative error of 10% compared the ground truth. Predictions based on two experimental datasets of AuNRs with correlated dark-field scattering

(DFS) and scanning electron microscopy (SEM) measurements achieve an accuracy when expressed as the root mean squared percentage error (RMSPE) of ~10%. We show that other decision tree-based ML models that increase in complexity do not lead to higher accuracy predictions for the AuNR dimensions. Further, analysis of other spectral features such as the maximum intensity (I_{max}) suggests that Γ and E_{res} are sufficient for size prediction, but for more complex characterization, intensity could be another input for improving the ability to use ML to correlate spectral properties with AuNR dimensions.

Experimental and Theoretical Methods

AuNR Sample Preparation. Two different size distributions of chemically synthesized AuNRs, Sample 1 (small AuNRs: $29 \pm 2 \times 78 \pm 9$ nm) and Sample 2 (large AuNRs: $63 \pm 4 \times 151 \pm 10$ nm) were used to test the predictive power of the DTR on experimental data (Figure 1A). Figures 1B and 1C display experimental DFS spectra of representative AuNRs from each sample. Increasing AuNR size introduces significant broadening of Γ while E_{res} redshifts, especially when considering the actual aspect ratios of 3.2 and 1.9 for the small (Figure 1B) and large (Figure 1C) AuNRs, respectively. Small AuNRs were synthesized using a modified seed-mediated growth process developed by Ye *et al*.[59] and large AuNRs were obtained via a synthesis method developed by Ming *et al.*[60] Details of the synthesis protocols for these two samples and their structural characterization are described in previous publications.[28, 61] Quartz substrates, indexed with an evaporated gold film pattern for correlated optical and electron microscopy, were cleaned with O_2 plasma for 2 minutes.[61] AuNRs were then spin coated on the indexed quartz slides for 60 seconds at 2500 rpm to achieve single particle coverage.

Correlated SEM and DFS. For single particle DFS measurements, we used a home-built setup based on an inverted microscope (Zeiss Axio Observer.D1m) with a 50× air objective having a 0.8 numerical aperture (Zeiss EC Epiplan-Neofluar). The excitation light focused on the sample with an oil immersion dark-field condenser was produced by a halogen lamp (Zeiss HAL 100). The scattered light passed through a pinhole with a 50 μm diameter (Thorlabs P50S) to achieve a confocal geometry. DFS images were constructed by moving the sample with a piezo scanning stage (Physik Instrumente P-517.3CL) and detecting the spatially filtered light on an avalanche photodiode (APD, PerkinElmer SPCM-AQRH-15). Single particle DFS spectra of the imaged particles were captured by redirecting the signal of each particle to a spectrometer (Shamrock SR193i-A) connected to a charge-coupled device (CCD) camera (Andor iDus 420 BEX2-DD). Spectral background noise was recorded with the same integration time of 3 seconds as used for the spectra and obtained from an area near the AuNR where no other nanoparticles were located. Furthermore, spectra were corrected for the white light spectrum from the halogen lamp, obtained by switching to the transmitted light mode of the condenser and recording the spectrum with the same CCD camera. Our confocal DFS setup yielded spectra with high signal-to-noise ratios (Sample 1: 154, Sample 2: 904), allowing for accurate fitting to a Lorentzian function (see Figures 1B and 1C). After all optical measurements, correlated SEM images were taken using a FEI Quanta 400 ESEM FEG in low-vacuum mode operating at a voltage of 30 kV with a final resolution of ~1.5 nm. AuNR dimensions were determined from these correlated SEM images for all individual AuNRs.

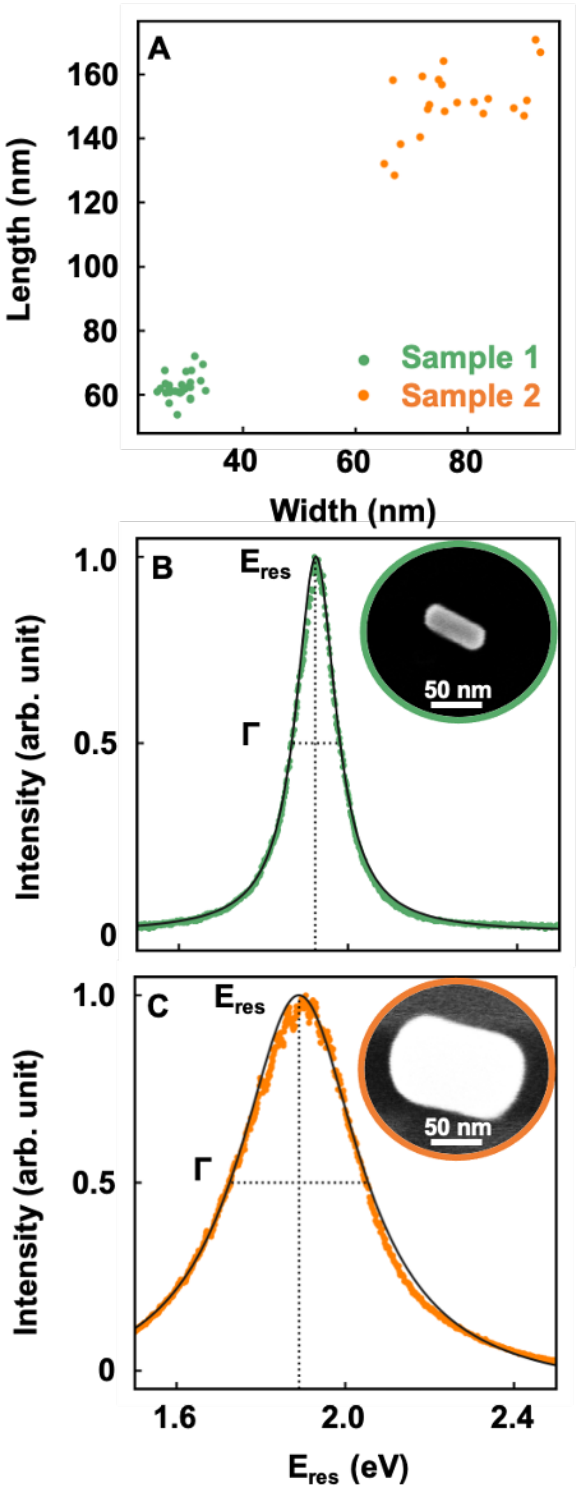

Figure 1: AuNR sample characterization. (A) Distributions of width and length of Sample 1 and Sample 2. Representative DFS spectra of a AuNR from Sample 1 (B) and one from Sample 2 (C) and their correlated SEM images given as insets. The solid black lines are Lorentzian fits of the spectra while vertical and horizontal lines mark E_{res} and Γ, respectively.

FDTD Simulations. The commercial software package Lumerical FDTD Solutions was employed to create a dataset of 576 spectrally resolved scattering cross sections of AuNRs to be subsampled and used as training and validation data (see Figure S1 for the width and length distributions). The geometry was approximated as a hemisphere capped gold cylinder surrounded by a 3.5 nm cetyltrimethylammonium bromide shell with a refractive index of 1.44 to account for the ligand molecules.[62] We employed the bulk gold dielectric function measured by Johnson and Christy to describe the AuNRs[63] sitting on a semi-infinite quartz substrate with a refractive index of 1.52.[62] We illuminated the AuNRs using a total-field scattered-field source with a normal incidence wave vector using a 0.5 nm computational

mesh size. We used default convergence criteria with perfectly matched layers to avoid errors arising from reflections at the boundaries.

Optical Feature Extraction. Γ and E_{res} of the longitudinal surface plasmon resonance were selected as input features for the model (Figures 2A and 2B), as previous research has indicated that they are strongly correlated to AuNR dimensions.[27, 28, 31, 35, 64] Three datasets were created to build the decision tree: training, validation, and testing. Training and validation data were sampled from a library of 576 FDTD simulated spectra where E_{res} and Γ were correlated to AuNR width and length. The testing data was comprised of 46 pairs of correlated experimental optical spectra and SEM measurements, providing real size measurements correlated to the trained input features E_{res} and Γ. Simulated spectra resembling data in the testing data were excluded from the training and validation data. All experimental and simulated spectra were fit with a Lorentzian function to obtain E_{res} and Γ. Spectra that could not be fit with a Lorentzian due to peaks trailing outside the range of measured wavelengths were excluded.

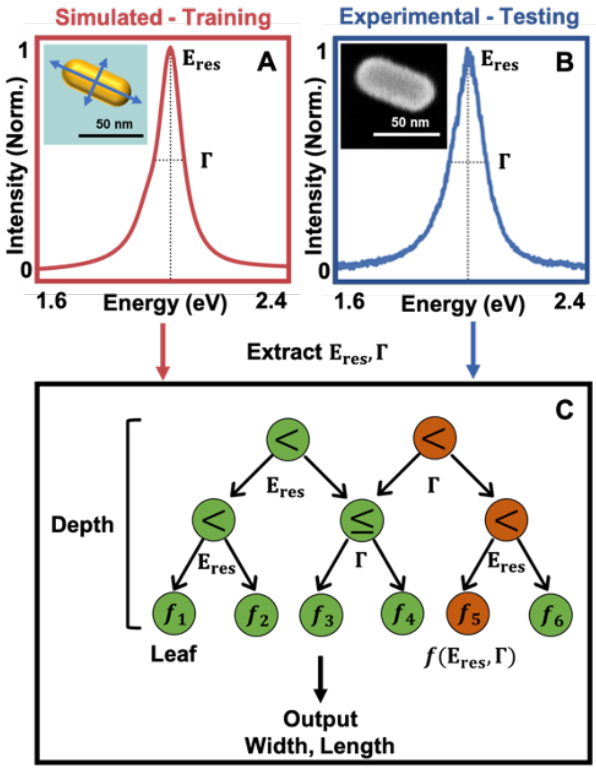

Figure 2: Data flow and representative schematic of the DTR model. (A) FDTD simulated AuNR DFS spectrum with two key features, E_{res} and Γ annotated on the graph. (B) Experimental DFS spectrum with matching annotations and correlated SEM image shown in the inset. (C) A schematic of the DTR algorithm predicting width and length of a AuNR by assessing E_{res} or Γ through three layers of decision nodes, two representing branch conditions and one being length/width assignment. Final decision nodes correspond to a linear function f(E_{res}, Γ) that can predict nanorod dimensions for that range of E_{res} and Γ.

Decision Tree Construction. The decision tree was constructed through recursive partitioning of the Γ and E_{res} feature space to map similar outputs to matching input feature combinations. Mapping was achieved through construction of several layers of decision nodes, each with a machine-learned pivot value that makes a greater-than/less-than comparison for a single feature (Figure 2C). Teaching the decision tree using feature combinations with known outcomes, referred to as training data,[65] determines the pivot values for each decision node and develops the branching conditions necessary to map different feature combinations to expected AuNR dimensions. Hyperparameters are user defined values that determine how a model learns patterns from training data and guides the structure of the decision tree in terms of number of layers and number of decision nodes per layer.[65] All hyperparameters were tuned to find the best trade-off between the number of layers, number of decision nodes per layer, and highest accuracy for training data. Here, five layers were sufficient to predict AuNR width and eight layers to predict AuNR length, with the requirement that each terminal decision node contained at least one sample. The hyperparameters of each model

were optimized using the machine learning library PyCaret (https://pycaret.org) and grid search,[65] which exhaustively generate the appropriate hyperparameters from a grid of hyperparameter values (see Table S1 for hyperparameters of other models). The following decision tree models were tested to compare prediction performance: Decision Tree Regressor (DTR),[57, 58] Random Forest Regressor (RFR),[66] Gradient Boosting Regressor (GBR),[67] XGBoost Regressor (XGB),[68] CatBoost Regressor (CBR)[69] and LightGBM Regressor (LGBM).[70] All models were implemented in Python, leveraging code provided by Scikit-learn.[71] After implementation, all models were compared based on the accuracy of predictions in the testing step in order to finalize the model selection (see below for a discussion on the comparison in accuracy). As an example of computational time needed, training the DTR took 3.58 ms $\pm$ 170 μs and testing 20 spectra 1.48 ms $\pm$ 52 μs on a laptop computer running Mac OS Big Sur (Version 11.4) with a 2.3 GHz Quad-Core Intel Core i7 processor and 16 GB of memory. An executable program based on our ML algorithm can be accessed at http://sizeprediction.rice.edu (see the Supporting Information for a user manual). The original code named "AuNR_DTR" is furthermore available for download through a GitHub repository (https://github.com/LandesLab/AuNR_DTR).

Results and Discussion

The prediction accuracy of our DTR converged using a notably small training dataset (~450 spectra), indicating that a simple relationship between our input features and AuNR dimensions must exist.[72, 73] One key concern in a ML implementation is the possibility of over/under fitting due to the limited scope of training data. We utilized ten-fold cross-validation on increasing data size to illustrate the generalizability of the model.[65] Here, a subset of the simulated spectra were randomly selected and used for cross-validation. The pool of simulated spectra was divided into ten unique subsets. Nine subsets were selected to train the model, while the remaining subset was used as validation data. The process of training/validating the model was repeated ten times where each iteration used a new combination of nine training subsets and one validation subset. Similar model output between different combinations of training/validation data indicate that the model is not skewed by the dataset and can be generalized to experimental results. To quantify the accuracy of our model, the RMSPE (the square root of the mean square of the relative error over a set of predictions) was averaged over all ten iterations of validation to form learning curves (see Table S2 for the definition of RMSPE).[56] The learning curves generated by cross-validation detect over/under fitting by examining the convergence of the model error based on the number of samples in our data.

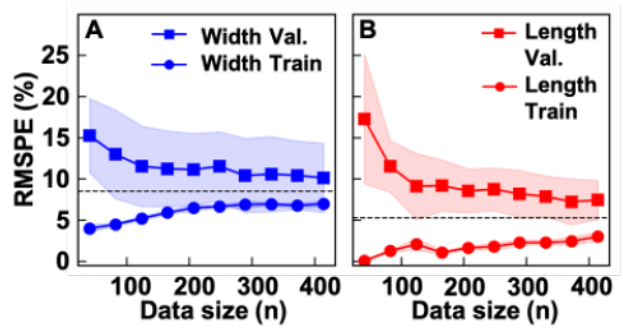

Figure 3: Learning curves for the decision tree model performance on simulated data. RMSPE for (A) width and (B) length as a function of the data size. Validation curves are represented by squares and training curves are represented by circles. The shaded areas around each curve were generated by ten-fold cross-validation. Error curves converge at 8.5% and 5.3% RMSPE for the width and length, respectively.

Figure 3 illustrates the convergence of training and validation learning curves to a shared asymptotic bound around 300 data points (see Figure S2 for the learning curves of other models). The prediction error stabilized at 8.5 % for the width (Figure 3A) and 5.3 % for the length (Figure 3B) for both training and validation data. Reaching a convergent error of <9% with such a small dataset implies that the relationship between spectral shape and AuNR size is simple enough to be captured using just two features, Γ and E_{res}. However, the correlation between features, a factor avoided through the pattern recognition of a decision tree, complicates the implementation of a linear relationship between spectral features and AuNR dimensions.[74]

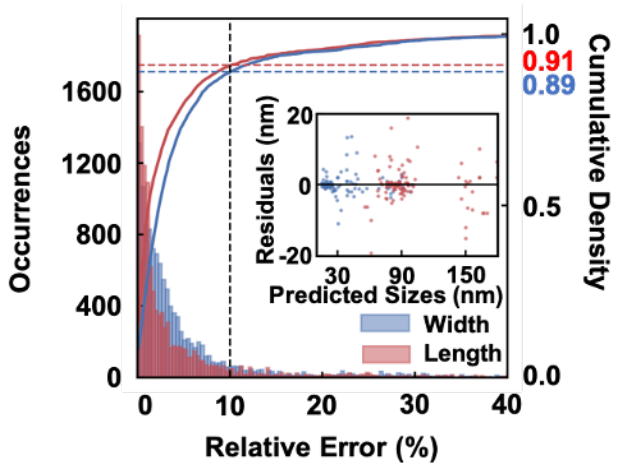

Figure 4: Evaluation of the model on simulated validation data. The histograms (bars, left y-axis) and cumulative densities (lines, right y-axis) of relative errors of width (blue) and length (red) for FDTD simulated validation data. Note that we had a total of 576 simulated data and randomly made 80% the training data and 20% the validation data. The horizontal dashed lines of width (blue) and length (red) indicate exact values of cumulative density where each population reaches 10 % relative error (vertical dashed black line). The inset shows the residuals for the predicted width and length at the 100th cycle compared to true sizes.

Analysis of the validation results in Figure 4 demonstrates that the model predicts AuNR dimensions with <10% relative error on 90% of all samples. To better understand the results of our ML model, we aggregated all prediction results from the ten-fold validation process into histograms based on the relative error of the predictions from the true values provided by simulated data. Figure 4 presents the distribution of relative errors for AuNR dimensions used in the FDTD simulations with annotations denoting the percentage of the population achieving a relative error of <10 %. Predictions for AuNR length are generally more accurate than predictions

for width, likely a result of the higher sensitivity of the longitudinal surface plasmon resonance to AuNR length.[15] Two key factors in the training data of a ML model are the breadth of coverage for different features and the skewing of data towards specific feature combinations. Both factors can be assessed as a function of prediction error over several iterations of training/validating and analysis of outliers, respectively. Error statistics were calculated by retraining the DTR 100 times using different subsets of 80% of the total 576 simulated spectra and validating against the remaining 20%. Variations in structure due to randomness in training were shown to have no effect on the quality of prediction. Here, low errors indicate that the dataset used for training adequately describes the range of feature combinations under investigation and that our results are not due to sampling errors between training and validation data. Regarding outliers, the inset of Figure 4 illustrates that the prediction outliers are evenly distributed over sizes, indicating that the decision tree accuracy is not biased by AuNR size.

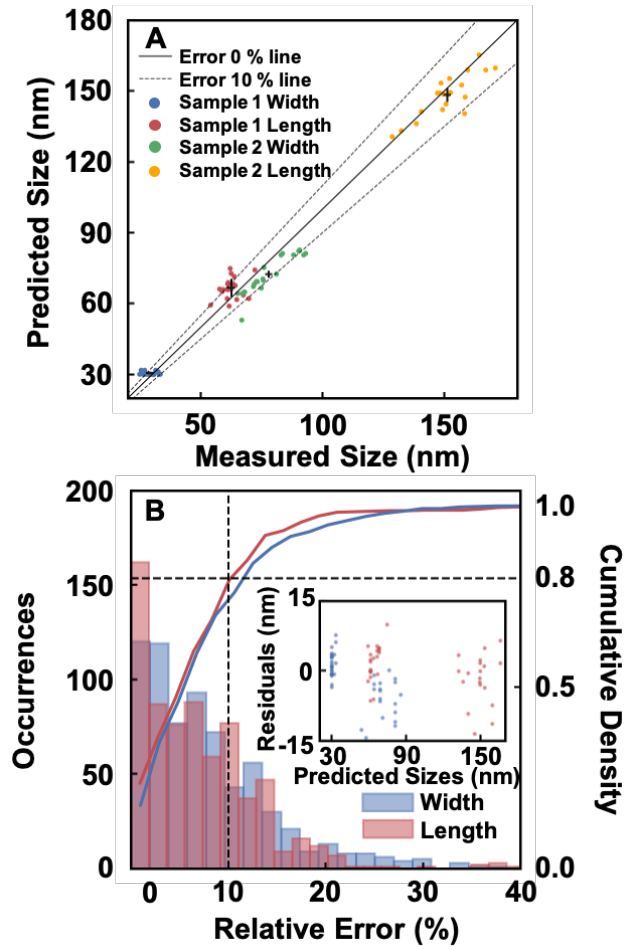

Figure 5: Evaluation of the model on experimental data. (A) Measured (x-axis) vs. predicted (y-axis) size scatter plot for width and length of 26 AuNRs in Sample 1 and 20 AuNRs in Sample 2. Error bars are located at the average of the dataset and are calculated from the error in the SEM measurement and the aggregate of 15 trained DTRs performing 15 independent predictions for the same experimental spectra. Each of the 15 DTRs were trained with 461 simulated spectra chosen randomly from the entire dataset of 576, with spectra matching the experiments excluded. Dashed lines denote ±10% error in prediction (width: 71.7%; length: 76.1%). (B) The histograms (bars, left y-axis) and cumulative densities (lines, right y-axis) of relative errors of width (blue) and length (red) for both samples combined. Note that in this case the 15 independent predictions for each AuNR were not averaged. The vertical dashed line denotes relative error of 10% and the horizontal dashed line denotes cumulative density of 0.8. The exact points of intersection for 10% relative error appear at cumulative densities of 0.74 for the width and 0.78 for the length. The inset shows the residuals for the predicted width and length at the 15th cycle compared to true values determined by SEM.

The DTR predicts experimental AuNR width and length over a broad range of sizes (Figure 5), suggesting that simulations are sufficient to learn the correlation between scattering spectra and AuNR dimensions. After training on 461 (80% of 576) simulated spectra, the model was tested by predicting the width and length from experimental DFS spectra compared to correlated SEM measurements. Figure 5A compares the prediction to sizes measured via SEM for Samples 1 and 2 (see Figure S4 for additional testing of experimental datasets containing a mixture of AuNR sizes). Statistics were generated by performing predictions with 15 iterations of the decision tree and averaging the predicted sizes. Error bars in Figure 5A are representative of each experimental dataset and are the average of the standard deviations for each prediction (Sample 1: width: ± 0.73 nm, length: ±

3.91 nm and Sample 2: width: ± 1.44 nm, length: ± 3.10 nm). Variability in prediction results based on the number of iterations is discussed in Figure S3.

Averaging 15 independent predictions for the width and length of each of the 46 experimental AuNR spectra, we find that 74% of the predicted AuNR dimensions averaged over width and length are within a relative error of 10% compared to their SEM measured sizes (Figures 5A). Increased accuracy over a wider range of sizes, compared to the reported method,[31] is likely because decision trees natively incorporate correlations between variables into the decision-making process,[57] eliminating the need for feature independence required by other regressive methods. Although decision trees are a discriminative model that provides hard boundaries for classification,[57] they do not offer mechanistic insight into how perturbations in E_{res} and Γ reflect changing AuNR dimensions. Relating feature values to ground truth physical chemistry is easier using regressive methods, which can connect results directly to experimental quantities in the form of weights to a fitted function, even if there are limitations to the range of predictable values. The selection of a classification method over a regressive method then represents a trade-off of accuracy at the detriment of interpretability.

The DTR gives similar prediction accuracy for experimental testing data as for simulated validation data. Figure 5B, an analog of Figure 4, shows the histogram of relative errors of each width and length prediction for experimental data. Transitioning to predictions on experimental data only incurs a modest decrease in accuracy, with 76% of all predictions averaged over width and length achieving <10% error. Note that the histogram includes all predicted values obtained from 15 independently trained decisions trees and no averaging over these 15 iterations was performed unlike for Figure 5A. The slight difference in the percentage of AuNRs having a relative error <10% when comparing Figure 5A and Figure 5B likely reflects that the sizes predicted for a

subset of AuNRs had a greater variance among the different decision trees, as can be seen from the distribution in Figure 5B extending to relative errors of 40%. Finally, when the data in Figure 5B is expressed in terms of RMSPE, accuracies of the width and length for Sample 1 are 11.4 ± 1.9% and 12.0 ± 3.1%, respectively, while the corresponding values for Sample 2 are 8.7 ± 1.1% and 5.0 ± 1.1 %, compared to 9.7 ± 1.8% for the width and 9.2 ± 2.4% for the length when using simulated spectra for validation (Figure 4). Overall, this analysis demonstrates that ML predicts the dimensions of gold nanorods within ~10% of their true value over a large range of sizes.

The sources of the greater error compared to validation of simulated spectra are likely due to real-world considerations not included in the simulated training data like signal-to-noise ratio and non-ideal AuNRs morphologies.[75] Decision tree predictions could be improved through the inclusion of experimental data in the training process, especially if the data is sampled from the instrument used to collect testing data. In doing so, correlations between features of interest like E_{res} and Γ, driven by experimental measurement conditions, could be anticipated in the model and subsequently improve the prediction accuracy. However, the fact that experimental predictions approach an error limit very similar to that found during model validation further suggests that FDTD spectra are accurate approximations of real-world results. It is reasonable to expect predictions to be less accurate when shifting to testing from validation data, but our model still provides comparably accurate predictions. In addition to the inclusion of experimental spectra in the training data it could be further refined by also increasing the total amount of training data available spanning an even wider range of dimensions. Doing so could allow the DTR to categorize a wider range of feature-size relationships.

Figure 6 compares the performance of linear regression against DTR and other decision tree-based models using the metrics of R^2 and RMSPE (see Table S2 for the definition of R^2) for both Sample 1 and Sample 2. In all cases, decision tree-based models outperform linear regression[65] in both metrics. Here, we see that AuNR sizes in Sample 2 could be predicted with higher accuracy than those in Sample 1. As we show below in Figure 7, this increased accuracy for the larger AuNRs is due to larger linewidths being more beneficial for accurate size predictions. We conclude that the relationship between spectral features and AuNR dimensions is non-linear but not prohibitively complex, as a simple DTR using only two features achieves higher accuracy than other tree-based models that use higher complexity decision making. While linear models are easier to interpret for mechanistic insights, accurate predictions based on non-linear DTRs rely directly on recognition of the underlying patterns among features in the data. It is important to note that size predictions obtained from polynomial

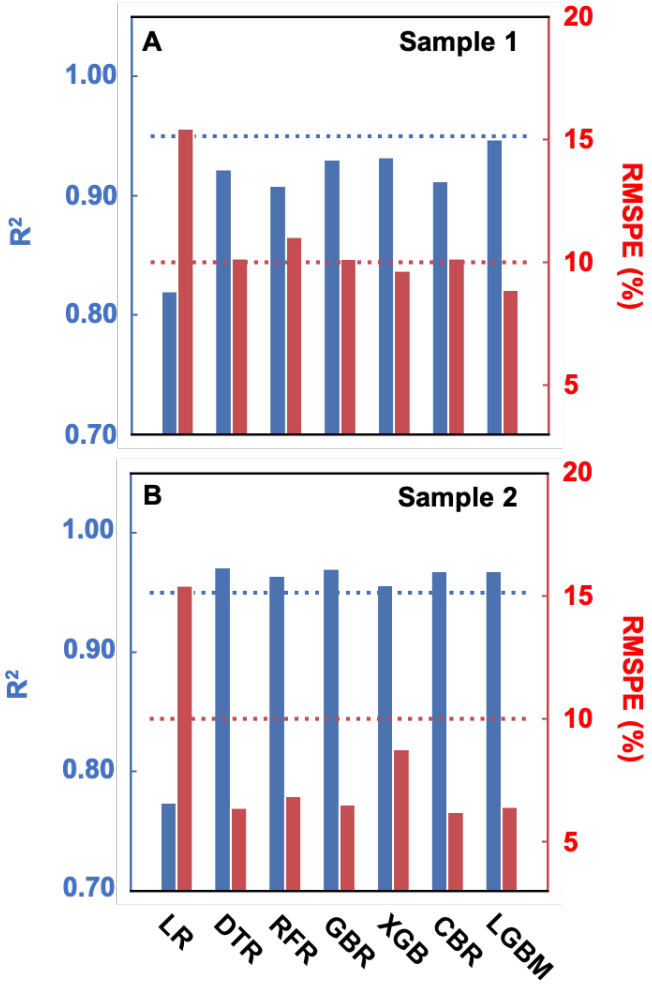

Figure 6: Statistical indices evaluating several different methods for predicting AuNR size from experimental spectra. The accuracy of several decision tree-based models compared to the linear regression (LR) prediction. The models tested include DTR, RFR, GBR, XGB, CBR, and LGBM for (A) Sample 1 and (B) Sample 2. Statistical indices were calculated for from all 46 predictions of AuNR width and length combined. The blue dotted lines mark $R^2 = 0.95$ and the red dotted lines mark RMSPE = 10%.

interpolation of our simulated spectra and tested with Sample 1 and Sample 2 resulted in RMSPE values exceeding 50% (Table S3). This difference might be attributed to the compatibility of our simulated dataset with conventional interpolation methods because interpolation requires systematically varied data points to cover the entire range of AuNR aspect ratios without any gaps,[31] while our simulated spectra were generated for a more random distribution of sizes (Figure S1).

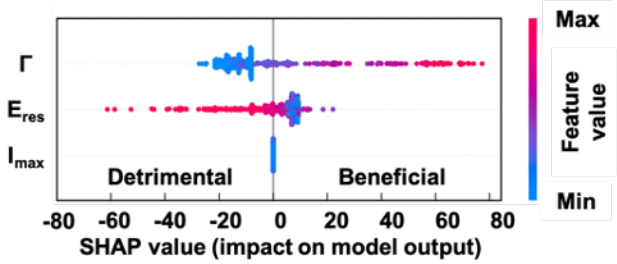

Figure 7: Impact of feature value on model prediction for simulated data. SHarply Additive exPlanation (SHAP) values for the spectral features Γ, E_{res}, and I_{max} in the order of impact on prediction of AuNR dimensions from the DTR. The red-blue colormap represents larger/smaller values of Γ and E_{res}, normalized to the range between the maximum and minimum values of the feature in the dataset. Negative/Positive SHAP value is detrimental/beneficial for the prediction, respectively.

Prediction accuracy depends conditionally on the values of Γ and E_{res} while I_{max} has no impact on the model (Figure 7). Model success is correlated to the composite of all features selected, as the values of some features can reduce the accuracy of predictions. One way of measuring the contribution of different features to a ML model is to use SHarply Additive exPlanation (SHAP) values (see Table S2 for the definition of SHAP).[76] In general, a positive or negative SHAP value corresponds to a feature being beneficial or detrimental to model accuracy, respectively. Figure 7 shows SHAP values calculated from training data used in Figure 4, illustrating a correlation between the value of the feature (red-blue gradient) and the contribution to the model. SHAP values demonstrate that the larger Γ values in the distribution provided the greatest improvement in model prediction accuracy. Broader linewidths are indicative of larger AuNRs and likely serve as a discriminator for the aspect ratio when E_{res} values are similar. Larger E_{res} values proved detrimental for model prediction, likely because blue-shifting of E_{res} causes

spectral overlap with the interband transitions of gold near the *L* symmetry point (~2.4 eV), resulting in deviations from a Lorentzian spectral line shape.[13, 77, 78] The value of I_{max} was found to have no discriminatory value, and as such was not included in the analysis presented in Figures 3-6. One reason is that I_{max} is not only affected by the shape of the AuNR but is also dependent on instrumental settings like source power and integration time. While I_{max} scales with increasing AuNR size in simulation, incorporating it as a feature in training data would require normalization. Such normalization could potentially be achieved by always measuring an internal standard on the same sample substrate (e.g., gold nanospheres or polystyrene beads) and evaluating I_{max} as a ratio against this standard. Inclusion of other spectral features that are independent of instrumental contributions, such as other statistical moments of the Lorentzian like skewness or excess, could potentially increase the predictive power of the DTR though.

Conclusions

We trained a DTR model with simulated spectra, allowing accurate predictions of AuNR sizes, in lieu of correlated electron microscopy. The DTR was trained using a relatively small dataset (~450) of scattering spectra obtained from FDTD simulations of AuNRs to correlate Γ and E_{res} with the AuNR width and length. Our method predicts the width and length of AuNRs with within ~10% of their true value (RMSPE) over a large range of sizes Sample 1 for width 11.4 ± 1.9% and length 12.0 ± 3.1%: Sample 2 for width 8.7 ± 1.1% and length 5.0 ± 1.1% of the true value for samples covering widths from 25 nm to 93 nm and lengths from 54 to 171 nm. Even a training dataset of 200 performed well yielding only slightly larger RMSPE values for the same set of experimental AuNR spectra (Figure S5), highlighting the novelty of our approach that only a relatively small amount of training data is needed. Importantly, we deduced that the relationship

between a set of just two spectral features (Γ and E_{res}) and AuNR sizes is non-linear but can be captured using a relatively simple decision tree. ML can bridge the knowledge gap between optical measurements and morphological features through pattern recognition from simulations and incorporation of experimental correlated values. We expect that this method of ML guided size extraction from optical properties will allow for real time, *in situ* size determination of single AuNR dimensions since our single particle hyperspectral imaging setup records spectra with a millisecond time resolution[79] that is compatible with the processing time of our algorithm. This speed of acquisition and processing should therefore prove useful for the size predictions of AuNRs undergoing diffusion or irreversible shape changes. Furthermore, the simple correlation between DFS features and AuNR dimensions indicates that our ML approach could likely be extended to predict the dimensions of other nanoparticles shapes, such as spheres, triangles, or cubes as well as mixtures of different shapes and nanoparticles made from other metals. However, a sufficiently large parameter space of optical features would need to be trained, while overlapping plasmon modes creating complex line shapes that make feature extraction from experimental spectra difficult should be minimized. Ultimately these considerations will present limitations of our ML approach.

Supporting Information Description

Size and feature distributions of simulated spectra, learning curves of other models, prediction variation per iteration for plots in Figure 5, additional testing of the model on AuNR populations with mixed sizes, analysis for using only 200 training datasets in Figure 3, 4, and 5, evaluation

metrics, hyperparameters tuning of other models, comparisons of RMSPE between interpolation polynomials and DTR, and GUI overview.

Author Information

Corresponding Authors

Stephan Link and Christy F. Landes

Email: slink@rice.edu, cflandes@rice.edu

Present Addresses

[†]Department of Electrical and System Engineering, University of Pennsylvania, 200 South 33rd Street, Philadelphia, Pennsylvania 19104, USA.

Author Contributions

*These authors contributed equally

Acknowledgments

This work was primarily funded by the Army Research Office (Grant No. W911NF1910363), supporting K.S. C.F.L., who contributed project direction, data interpretation, and writing, was also partially supported by the National Science Foundation (NSF CHE-1808382) and thanks the Robert A. Welch Foundation (C-1787) for financial support of R.B. S.L. also acknowledges financial support through a grant from to the Robert A. Welch Foundation (C-1664), which supported B.O. L.D.C.B. acknowledges that this material is based upon work supported by the National Science Foundation Graduate Research Fellowship Program (Grant 1842494). This work was conducted in part using resources of the Shared Equipment Authority at Rice University.

References:

1. Clavero, C., Plasmon-Induced Hot-Electron Generation at Nanoparticle/Metal-Oxide Interfaces for Photovoltaic and Photocatalytic Devices. *Nat. Photonics* **2014,** *8*, 95-103.
2. Atwater, H. A.; Polman, A., Plasmonics for Improved Photovoltaic Devices. *Nat. Mater.* **2010,** *9*, 205-213.
3. Linic, S.; Christopher, P.; Ingram, D. B., Plasmonic-Metal Nanostructures for Efficient Conversion of Solar to Chemical Energy. *Nat. Mater.* **2011,** *10*, 911-921.
4. Wu, S.; Hogan, N.; Sheldon, M., Hot Electron Emission in Plasmonic Thermionic Converters. *ACS Energy Lett.* **2019,** *4*, 2508-2513.
5. Robatjazi, H.; Zhao, H.; Swearer, D. F.; Hogan, N. J.; Zhou, L.; Alabastri, A.; McClain, M. J.; Nordlander, P.; Halas, N. J., Plasmon-Induced Selective Carbon Dioxide Conversion on Earth-Abundant Aluminum-Cuprous Oxide Antenna-Reactor Nanoparticles. *Nat. Commun.* **2017,** *8*, 27.
6. Mubeen, S.; Lee, J.; Singh, N.; Kramer, S.; Stucky, G. D.; Moskovits, M., An Autonomous Photosynthetic Device in Which All Charge Carriers Derive from Surface Plasmons. *Nat. Nanotechnol.* **2013,** *8*, 247-251.
7. Brongersma, M. L.; Halas, N. J.; Nordlander, P., Plasmon-Induced Hot Carrier Science and Technology. *Nat. Nanotechnol.* **2015,** *10*, 25-34.
8. Kim, Y.; Smith, J. G.; Jain, P. K., Harvesting Multiple Electron-Hole Pairs Generated through Plasmonic Excitation of Au Nanoparticles. *Nat. Chem.* **2018,** *10*, 763-769.
9. Kneipp, K.; Wang, Y.; Kneipp, H.; Perelman, L. T.; Itzkan, I.; Dasari, R.; Feld, M. S., Single Molecule Detection Using Surface-Enhanced Raman Scattering (Sers). *Phys. Rev. Lett.* **1997,** *78*, 1667-1670.
10. Wokaun, A.; Gordon, J. P.; Liao, P. F., Radiation Damping in Surface-Enhanced Raman-Scattering. *Phys. Rev. Lett.* **1982,** *48*, 957-960.
11. Fleischmann, M.; Hendra, P. J.; McQuillan, A. J., Raman-Spectra of Pyridine Adsorbed at a Silver Electrode. *Chem. Phys. Lett.* **1974,** *26*, 163-166.
12. Moskovits, M., Surface-Enhanced Spectroscopy. *Rev. Mod. Phys.* **1985,** *57*, 783-826.
13. Kreibig, U.; Vollmer, M., *Optical Properties of Metal Clusters*. Springer: Berlin, 1994.
14. Bohren, C. F.; Huffman, D. R., *Absorption and Scattering of Light by Small Particles* Wiley-VCH Verlaag GmbH & Co. KGaA: New York, 1983.
15. Link, S.; Mohamed, M. B.; El-Sayed, M. A., Simulation of the Optical Absorption Spectra of Gold Nanorods as a Function of Their Aspect Ratio and the Effect of the Medium Dielectric Constant. *J. Phys. Chem. B* **1999,** *103*, 3073-3077.
16. Kelly, K. L.; Coronado, E.; Zhao, L. L.; Schatz, G. C., The Optical Properties of Metal Nanoparticles: The Influence of Size, Shape, and Dielectric Environment. *J. Phys. Chem. B* **2003,** *107*, 668-677.
17. Slaughter, L. S.; Chang, W.-S.; Swanglap, P.; Tcherniak, A.; Khanal, B. P.; Zubarev, E. R.; Link, S., Single-Particle Spectroscopy of Gold Nanorods Beyond the Quasi-Static Limit: Varying the Width at Constant Aspect Ratio. *J. Phys. Chem. C* **2010,** *114*, 4934-4938.
18. Hartland, G. V., Optical Studies of Dynamics in Noble Metal Nanostructures. *Chem. Rev.* **2011,** *111*, 3858-3887.
19. Gaiduk, A.; Yorulmaz, M.; Orrit, M., Correlated Absorption and Photoluminescence of Single Gold Nanoparticles. *ChemPhysChem* **2011,** *12*, 1536-1541.

20. Sivun, D.; Vidal, C.; Munkhbat, B.; Arnold, N.; Klar, T. A.; Hrelescu, C., Anticorrelation of Photoluminescence from Gold Nanoparticle Dimers with Hot-Spot Intensity. *Nano Lett.* **2016,** *16*, 7203-7209.
21. Zhao, T.; Jarrett, J. W.; Johnson, J. S.; Park, K.; Vaia, R. A.; Knappenberger, K. L., Jr., Plasmon Dephasing in Gold Nanorods Studied Using Single-Nanoparticle Interferometric Nonlinear Optical Microscopy. *J. Phys. Chem. C* **2016,** *120*, 4071-4079.
22. Donehue, J. E.; Wertz, E.; Talicska, C. N.; Biteen, J. S., Plasmon-Enhanced Brightness and Photostability from Single Fluorescent Proteins Coupled to Gold Nanorods. *J. Phys. Chem. C* **2014,** *118*, 15027-15035.
23. Buurmans, I. L.; Weckhuysen, B. M., Heterogeneities of Individual Catalyst Particles in Space and Time as Monitored by Spectroscopy. *Nat. Chem.* **2012,** *4*, 873-886.
24. Byers, C. P.; Hoener, B. S.; Chang, W. S.; Yorulmaz, M.; Link, S.; Landes, C. F., Single-Particle Spectroscopy Reveals Heterogeneity in Electrochemical Tuning of the Localized Surface Plasmon. *J. Phys. Chem. B* **2014,** *118*, 14047-14055.
25. Murphy, C. J.; San, T. K.; Gole, A. M.; Orendorff, C. J.; Gao, J. X.; Gou, L.; Hunyadi, S. E.; Li, T., Anisotropic Metal Nanoparticles: Synthesis, Assembly, and Optical Applications. *J. Phys. Chem. B* **2005,** *109*, 13857-13870.
26. Olson, J.; Dominguez-Medina, S.; Hoggard, A.; Wang, L. Y.; Chang, W. S.; Link, S., Optical Characterization of Single Plasmonic Nanoparticles. *Chem. Soc. Rev.* **2015,** *44*, 40-57.
27. Lin, K.-Q.; Yi, J.; Hu, S.; Liu, B.-J.; Liu, J.-Y.; Wang, X.; Ren, B., Size Effect on Sers of Gold Nanorods Demonstrated Via Single Nanoparticle Spectroscopy. *J. Phys. Chem. C* **2016,** *120*, 20806-20813.
28. Ostovar, B.; Cai, Y.-Y.; Tauzin, L. J.; Lee, S. A.; Ahmadivand, A.; Zhang, R.; Nordlander, P.; Link, S., Increased Intraband Transitions in Smaller Gold Nanorods Enhance Light Emission. *ACS Nano* **2020,** *14*, 15757-15765.
29. Yang, L.; Yan, B.; Reinhard, B. M., Correlated Optical Spectroscopy and Transmission Electron Microscopy of Individual Hollow Nanoparticles and Their Dimers. *J. Phys. Chem. C* **2008,** *112*, 15989-15996.
30. Taylor, A.; Verhoef, R.; Beuwer, M.; Wang, Y.; Zijlstra, P., All-Optical Imaging of Gold Nanoparticle Geometry Using Super-Resolution Microscopy. *J. Phys. Chem. C* **2018,** *122*, 2336-2342.
31. Henkel, A.; Ye, W.; Khalavka, Y.; Neiser, A.; Lambertz, C.; Schmachtel, S.; Ahijado-Guzmán, R.; Sönnichsen, C., Narrowing the Plasmonic Sensitivity Distribution by Considering the Individual Size of Gold Nanorods. *J. Phys. Chem. C* **2018,** *122*, 10133-10137.
32. Sonnichsen, C.; Franzl, T.; Wilk, T.; von Plessen, G.; Feldmann, J.; Wilson, O.; Mulvaney, P., Drastic Reduction of Plasmon Damping in Gold Nanorods. *Phys. Rev. Lett.* **2002,** *88*.
33. Becker, J.; Schubert, O.; Sonnichsen, C., Gold Nanoparticle Growth Monitored in Situ Using a Novel Fast Optical Single-Particle Spectroscopy Method. *Nano Lett.* **2007,** *7*, 1664-1669.
34. Novo, C.; Gomez, D.; Perez-Juste, J.; Zhang, Z.; Petrova, H.; Reismann, M.; Mulvaney, P.; Hartland, G. V., Contributions from Radiation Damping and Surface Scattering to the Linewidth of the Longitudinal Plasmon Band of Gold Nanorods: A Single Particle Study. *Phys. Chem. Chem. Phys.* **2006,** *8*, 3540-3546.
35. Berciaud, S.; Cognet, L.; Tamarat, P.; Lounis, B., Observation of Intrinsic Size Effects in the Optical Response of Individual Gold Nanoparticles. *Nano Lett.* **2005,** *5*, 515-518.

36. Brown, K. A.; Brittman, S.; Maccaferri, N.; Jariwala, D.; Celano, U., Machine Learning in Nanoscience: Big Data at Small Scales. *Nano Lett.* **2020,** *20*, 2-10.
37. Barnard, A. S.; Motevalli, B.; Parker, A. J.; Fischer, J. M.; Feigl, C. A.; Opletal, G., Nanoinformatics, and the Big Challenges for the Science of Small Things. *Nanoscale* **2019,** *11*, 19190-19201.
38. Yang, W.; Fidelis, T. T.; Sun, W. H., Machine Learning in Catalysis, from Proposal to Practicing. *ACS Omega* **2020,** *5*, 83-88.
39. Toyao, T.; Maeno, Z.; Takakusagi, S.; Kamachi, T.; Takigawa, I.; Shimizu, K.-i., Machine Learning for Catalysis Informatics: Recent Applications and Prospects. *ACS Catal.* **2019,** *10*, 2260-2297.
40. Parker, A. J.; Opletal, G.; Barnard, A. S., Classification of Platinum Nanoparticle Catalysts Using Machine Learning. *J. Appl. Phys.* **2020,** *128*.
41. Goldsmith, B. R.; Esterhuizen, J.; Liu, J. X.; Bartel, C. J.; Sutton, C., Machine Learning for Heterogeneous Catalyst Design and Discovery. *AIChE J.* **2018,** *64*, 2311-2323.
42. Barnard, A. S.; Opletal, G., Selecting Machine Learning Models for Metallic Nanoparticles. *Nano Futures* **2020,** *4*.
43. Sun, B.; Fernandez, M.; Barnard, A. S., Machine Learning for Silver Nanoparticle Electron Transfer Property Prediction. *J. Chem. Inf. Model.* **2017,** *57*, 2413-2423.
44. Panapitiya, G.; Avendano-Franco, G.; Ren, P.; Wen, X.; Li, Y.; Lewis, J. P., Machine-Learning Prediction of Co Adsorption in Thiolated, Ag-Alloyed Au Nanoclusters. *J. Am. Chem. Soc.* **2018,** *140*, 17508-17514.
45. Takahashi, K.; Takahashi, L., Data Driven Determination in Growth of Silver from Clusters to Nanoparticles and Bulk. *J. Phys. Chem. Lett.* **2019,** *10*, 4063-4068.
46. Wang, X.; Li, J.; Ha, H. D.; Dahl, J. C.; Ondry, J. C.; Moreno-Hernandez, I.; Head-Gordon, T.; Alivisatos, A. P., Autodetect-Mnp: An Unsupervised Machine Learning Algorithm for Automated Analysis of Transmission Electron Microscope Images of Metal Nanoparticles. *JACS Au* **2021,** *1*, 316-327.
47. Jamali, V.; Hargus, C.; Ben-Moshe, A.; Aghazadeh, A.; Ha, H. D.; Mandadapu, K. K.; Alivisatos, A. P., Anomalous Nanoparticle Surface Diffusion in Lctem Is Revealed by Deep Learning-Assisted Analysis. *Proc. Natl. Acad. Sci. U. S. A.* **2021,** *118*, e2017616118.
48. Moon, G.; Son, T.; Lee, H.; Kim, D., Deep Learning Approach for Enhanced Detection of Surface Plasmon Scattering. *Anal Chem* **2019,** *91*, 9538-9545.
49. Pashkov, D. M.; Guda, A. A.; Kirichkov, M. V.; Guda, S. A.; Martini, A.; Soldatov, S. A.; Soldatov, A. V., Quantitative Analysis of the Uv-Vis Spectra for Gold Nanoparticles Powered by Supervised Machine Learning. *J. Phys. Chem. C* **2021,** *125*, 8656-8666.
50. Timoshenko, J.; Lu, D. Y.; Lin, Y. W.; Frenkel, A. I., Supervised Machine-Learning-Based Determination of Three-Dimensional Structure of Metallic Nanoparticles. *J. Phys. Chem. Lett.* **2017,** *8*, 5091-5098.
51. Ballard, Z. S.; Shir, D.; Bhardwaj, A.; Bazargan, S.; Sathianathan, S.; Ozcan, A., Computational Sensing Using Low-Cost and Mobile Plasmonic Readers Designed by Machine Learning. *ACS Nano* **2017,** *11*, 2266-2274.
52. Liu, D.; Tan, Y.; Khoram, E.; Yu, Z., Training Deep Neural Networks for the Inverse Design of Nanophotonic Structures. *ACS Photonics* **2018,** *5*, 1365-1369.
53. Liu, Z. C.; Zhu, D. Y.; Raju, L.; Cai, W. S., Tackling Photonic Inverse Design with Machine Learning. *Adv. Sci.* **2021,** *8*.

54. Malkiel, I.; Mrejen, M.; Nagler, A.; Arieli, U.; Wolf, L.; Suchowski, H., Plasmonic Nanostructure Design and Characterization Via Deep Learning. *Light: Sci. Appl.* **2018,** *7*.
55. He, J.; He, C.; Zheng, C.; Wang, Q.; Ye, J., Plasmonic Nanoparticle Simulations and Inverse Design Using Machine Learning. *Nanoscale* **2019,** *11*, 17444-17459.
56. Bishop, C. M., *Pattern Recognition and Machine Learning*. Springer: New York, 2006.
57. Breiman, L.; Friedman, J.; Stone, C. J.; Olshen, R. A., *Classification and Regression Trees*. CRC Press: Boca Raton, FL, 1984.
58. Murphy, K. P., *Machine Learning: A Probabilistic Perspective*. Mit Press: Cambridge, 2012.
59. Ye, X.; Zheng, C.; Chen, J.; Gao, Y.; Murray, C. B., Using Binary Surfactant Mixtures to Simultaneously Improve the Dimensional Tunability and Monodispersity in the Seeded Growth of Gold Nanorods. *Nano Lett.* **2013,** *13*, 765-771.
60. Ming, T.; Feng, W.; Tang, Q.; Wang, F.; Sun, L.; Wang, J.; Yan, C., Growth of Tetrahexahedral Gold Nanocrystals with High-Index Facets. *J. Am. Chem. Soc.* **2009,** *131*, 16350-16351.
61. Cai, Y. Y.; Liu, J. G.; Tauzin, L. J.; Huang, D.; Sung, E.; Zhang, H.; Joplin, A.; Chang, W. S.; Nordlander, P.; Link, S., Photoluminescence of Gold Nanorods: Purcell Effect Enhanced Emission from Hot Carriers. *ACS Nano* **2018,** *12*, 976-985.
62. Martinsson, E.; Shahjamali, M. M.; Large, N.; Zaraee, N.; Zhou, Y.; Schatz, G. C.; Mirkin, C. A.; Aili, D., Influence of Surfactant Bilayers on the Refractive Index Sensitivity and Catalytic Properties of Anisotropic Gold Nanoparticles. *Small* **2016,** *12*, 330-342.
63. Johnson, P. B.; Christy, R. W., Optical Constants of the Noble Metals. *Phys. Rev. B* **1972,** *6*, 4370-4379.
64. Cai, Y.-Y.; Sung, E.; Zhang, R.; Tauzin, L. J.; Liu, J. G.; Ostovar, B.; Zhang, Y.; Chang, W.-S.; Nordlander, P.; Link, S., Anti-Stokes Emission from Hot Carriers in Gold Nanorods. *Nano Lett.* **2019,** *19*, 1067-1073.
65. Géron, A. l., *Hands-on Machine Learning with Scikit-Learn and Tensorflow : Concepts, Tools, and Techniques to Build Intelligent Systems*. First edition. ed.; O'Reilly Media: Sebastopol, CA, 2017.
66. Breiman, L., Randomforests. *Machine Learning* **2001,** *45*, 5-32.
67. Friedman, J. H., Greedy Function Approximation: A Gradient Boosting Machine. *Ann. Statist.* **2001,** *29*, 1189-1232.
68. Chen, T.; Guestrin, C. Xgboost: A Scalable Tree Boosting System 2016, p. arXiv:1603.02754. https://ui.adsabs.harvard.edu/abs/2016arXiv160302754C (accessed March 01, 2016).
69. Prokhorenkova, L.; Gusev, G.; Vorobev, A.; Veronika Dorogush, A.; Gulin, A. Catboost: Unbiased Boosting with Categorical Features 2017, p. arXiv:1706.09516. https://ui.adsabs.harvard.edu/abs/2017arXiv170609516P (accessed June 01, 2017).
70. Ke, G.; Meng, Q.; Finley, T.; Wang, T.; Chen, W.; Ma, W.; Ye, Q.; Liu, T.-Y. In *Lightgbm: A Highly Efficient Gradient Boosting Decision Tree*, Proceedings of the 31st International Conference on Neural Information Processing Systems, Long Beach, California, USA, Curran Associates Inc.: Long Beach, California, USA, 2017; pp 3149–3157.
71. Pedregosa, F.; Varoquaux, G.; Gramfort, A.; Michel, V.; Thirion, B.; Grisel, O.; Blondel, M.; Müller, A.; Nothman, J.; Louppe, G. *et. al.* Scikit-Learn: Machine Learning in Python 2012, p. arXiv:1201.0490. https://ui.adsabs.harvard.edu/abs/2012arXiv1201.0490P (accessed January 01, 2012).

72. Vabalas, A.; Gowen, E.; Poliakoff, E.; Casson, A. J., Machine Learning Algorithm Validation with a Limited Sample Size. *PLos One* **2019,** *14*.
73. Raudys, S. J.; Jain, A. K., Small Sample-Size Effects in Statistical Pattern-Recognition - Recommendations for Practitioners. *Ieee Transactions on Pattern Analysis and Machine Intelligence* **1991,** *13*, 252-264.
74. Strobl, C.; Boulesteix, A.-L.; Kneib, T.; Augustin, T.; Zeileis, A., Conditional Variable Importance for Random Forests. *BMC Bioinf.* **2008,** *9*.
75. Trügler, A.; Tinguely, J.-C.; Krenn, J. R.; Hohenau, A.; Hohenester, U., Influence of Surface Roughness on the Optical Properties of Plasmonic Nanoparticles. *Phys. Rev. B* **2011,** *83*.
76. Lundberg, S.; Lee, S.-I. A Unified Approach to Interpreting Model Predictions 2017, p. arXiv:1705.07874. https://ui.adsabs.harvard.edu/abs/2017arXiv170507874L (accessed May 01, 2017).
77. Guerrisi, M.; Rosei, R.; Winsemius, P., Splitting of Interband Absorption-Edge in Au. *Phys. Rev. B* **1975,** *12*, 557-563.
78. Winsemius, P.; Guerrisi, M.; Rosei, R., Splitting of Interband Absorption-Edge in Au - Temperature-Dependence. *Phys. Rev. B* **1975,** *12*, 4570-4572.
79. Kirchner, S. R.; Smith, K. W.; Hoener, B. S.; Collins, S. S. E.; Wang, W.; Cai, Y.-Y.; Kinnear, C.; Zhang, H.; Chang, W.-S.; Mulvaney, P.; Landes, C. F.; Link, S., Snapshot Hyperspectral Imaging (Shi) for Revealing Irreversible and Heterogeneous Plasmonic Processes. *J. Phys. Chem. C* **2018,** *122*, 6865-6875.

TOC graphic